Robust Extraction of the Optic Nerve Head in Optical Coherence Tomography

Artemas Herzog¹, Kim L. Boyer¹, and Cynthia Roberts²

¹ The Ohio State University
Signal Analysis and Machine Perception Laboratory
Department of Electrical and Computer Engineering
herzoga@ece.osu.edu, kim@ece.osu.edu

² Department of Ophthalmology
roberts.8@osu.edu

Abstract. Glaucoma is a leading cause of blindness. While glaucoma is a treatable and controllable disease, there is still no cure available. Early diagnosis is important in order to prevent severe vision loss. Many current diagnostic techniques are subjective and variable. This provides motivation for a more objective and repeatable method. Optical Coherence Tomography (OCT) is a relatively new imaging technique that is proving useful in diagnosing, monitoring, and studying glaucoma. OCT, like ultrasound, suffers from signal dependent noise which can make accurate, automatic segmentation of images difficult. In this article we propose a method to automatically extract the optic nerve and retinal boundaries from axial OCT scans through the optic nerve head. We also propose a method to automatically segment the curve to extract the nerve head profile that is important in diagnosing and monitoring glaucoma.

1 Introduction

Optical Coherence tomography (OCT) is a relatively new imaging technique [1]. While similar to ultrasound, OCT relies on the detection of backscattered light and time of flight information to produce high resolution, cross-sectional images. OCT has been particularly useful in biological imaging applications such as dermatology, cardiology, and ophthalmology [2, 3, 4]. Specifically in the ophthalmological case, OCT has been used for a variety of purposes which range from measuring corneal thickness in the anterior segment of the eye to measuring the retinal thickness in the posterior segment of the eye [5]. Although limited to relatively shallow imaging depths, approximately 2mm in retinal scans, OCT benefits from being a non-invasive procedure in ophthalmological imaging with a 5-10 micron axial resolution [6]. Thus detailed images of the retinal tissue structure can be obtained with the potential for high tolerance measurements.

Retinal nerve fiber layer thickness is a clinically important measurement in the diagnosis and monitoring of glaucoma [7]. Over time the retinal nerve fiber layer thickness around the optic nerve tends to decrease as nervous tissue is destroyed. It has been estimated that up to 40% of the nerve fiber can be destroyed

M. Šonka et al. (Eds.): CVAMIA-MMBIA 2004, LNCS 3117, pp. 395-407, 2004.

[©] Springer-Verlag Berlin Heidelberg 2004

before significant vision loss occurs [8]. The cup-to-disk ratio and the optic cup shape are also important indicators of glaucoma and optic nerve health; however, cup-to-disk ratio is an ill-defined term. The most popular way to measure the cup-to-disk ratio is through direct observation. Here the physician observes the optic nerve through fundus imaging and estimates what he/she believes the cup-to-disk ratio to be. This technique is subjective and variable and provides motivation for an objective method that is more accurate and repeatable. In this paper we propose a method to robustly extract the retinal and optic nerve head boundaries from axial OCT scans of the optic nerve head. With the boundaries extracted, we next propose a method for segmenting the optic cup from the retina and disk.

The eye is divided into two chambers, the anterior chamber and the posterior chamber. The posterior chamber is filled with a relatively homogenous, jelly like substance called the vitreous humor [9]. The retina is the anterior most tissue layer in the back of the posterior chamber. It is here that light rays are focused and processed before being sent via the optic nerve to the brain. We note that the top most layer of the retina is composed of nerve fibers. It is these nerve fibers that are destroyed due to glaucoma. The layer of tissue below the retina is a highly reflective layer called the choroid and is mostly composed of blood vessels which feed the back of the eye.

Finally, the optic disk is the area of the retina where the nerve fiber layers converge to form the optic nerve. The cup is the area of so-called empty space in the central region of the optic disk. In normal eyes the ratio of the cup area to the disk area (cup-to-disk ratio) is small (less than 0.6) [8]. In glaucomatous eyes, the death of nerve fibers causes the size of the cup to increase and thus the cup-to-disk ratio also increases. The shape of the cup can also provide an indicator as to whether or not an individual has glaucoma.

2 Optical Coherence Tomography

Optical Coherence Tomography is similar to ultrasound. Instead of sound, light is sent into a sample and the time of arrival and intensity of the backscattered light is used to form an image. However, because the speed of light is over a million times faster than the speed of sound, coherence based detection techniques are often chosen over nonlinear gating techniques and Kerr shutters [10].

In coherence based detection an interferometer is used to split the energy from a light source E(t) into a reference field $E_r(t)$ and a sample field $E_s(t)$. The sample field travels a total distance l_s and the reference field l_r . The two fields add together at the detector and the total detector photocurrent is

$$I_D \sim \frac{1}{4}|E_r|^2 + \frac{1}{4}|E_s|^2 + \frac{1}{2}|E_r E_s|\cos(2\frac{2\pi}{\lambda}\Delta l)$$
 (1)

where λ is the wavelength of the light source and

$$\Delta l = l_r - l_s \tag{2}$$

Thus (1) tells us that the intensity of the photocurrent oscillates as a function of the path length difference (2). It can be shown that when a low coherence source is used I_D becomes the cross-correlation function of the sample field with the reference field. The fields are correlated (i.e. interfere constructively) when Δl is less than the coherence length l_c and are uncorrelated otherwise. The coherence length is inversely proportional to the bandwidth of the light source. Because the sample field is relatively constant, we can control imaging depth by controlling the length of the reference beam. Our images were obtained using the OCT

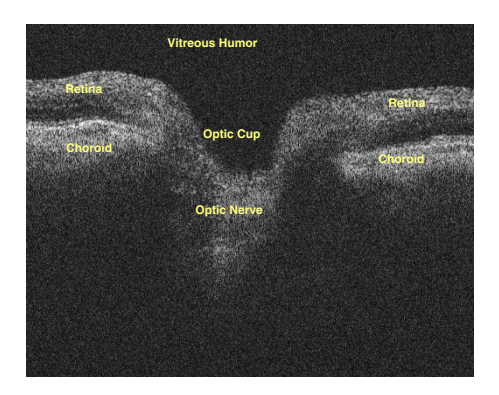


Fig. 1. A typical OCT scan through the optic nerve with labeled structures.

3000 from Zeiss-Humphrey. The typical scan consists of 512 A-scans where each A-scan consists of 1024 pixels. The axial resolution is $< 10 \mu m$ and the transverse resolution is dependent on the scan length. Fig. 1 shows a typical scan through the optic nerve head with various anatomical structures marked.

3 Theory

Segmentation of OCT images is a difficult task. Koozekanani et al. [11] proposed a Markov Boundary Model to extract the retinal boundaries from circular scans of the macula. While their method is robust on the macular region of the retina, the model they used fails in the optic nerve head region due to the significant anatomical differences. It is impractical to train a new Markov model because there is considerably more variation in the optic nerve head regions between subjects. We can still, though, rely on the assumption that the retinal/optic nerve head profile is smooth and that significant undulations in the retina are usually the result of eye movement. The optic disk surface also varies slowly, although considerably less so than the retina. We can assume that the imaging technician will discard the image if movement is severe enough to cause significant image distortion or large breaks in the profile. Likewise, if shadowing significantly reduces the visibility of entire image regions, the technician will again discard the images. However, less severe shadow effects, breaks, distortions, and artifacts

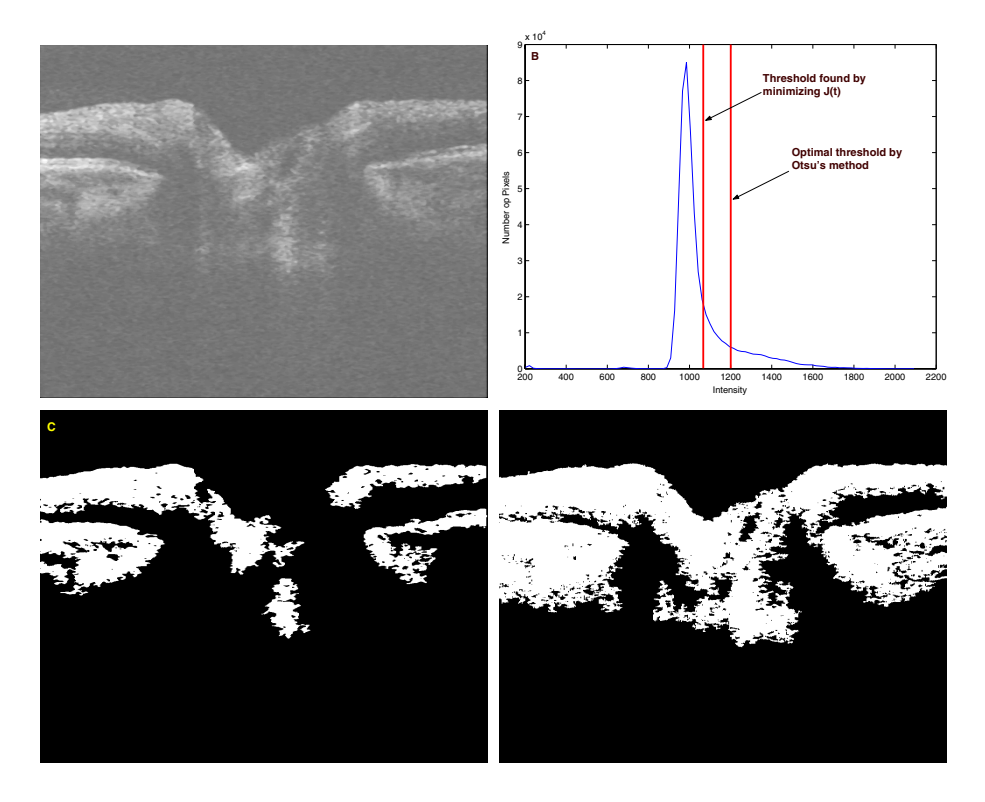


Fig. 2. (A) is a noise suppressed OCT scan. The image histogram is shown in (B) and shows the thresholds obtained using Otsu's method and our method. (C) is the thresholded image resulting from Otsu's method and (D) is the thresholded image using our method.

must be assumed likely and that the OCT technician will keep such images. Thus our method should be robust enough to handle such effects.

The most complicated problem with OCT images is the nonlinear, signal dependent noise that is inherent in coherence imaging techniques. This noise is called speckle due to its appearance in the images. Ultrasound and synthetic aperture radar imaging also suffer from this phenomenon. Speckle arises because of multiple backscattering and forward scattering within the sample volume [12]. Organic tissue is never homogenous and thus a sample volume is highly likely to have multiple scatterers (i.e cells, organelles, fibers, fluids ...). Speckle forms when light from these multiple scatterers reaches the detector out of phase within the coherence time of the source. Thus multiple backscattering causes constructive and destructive interference that alters the wave shape incident the detector. Speckle is both a signal carrier, in that it reveals information about the underlying microstructure, and a source of noise. While distinguishing between noise speckle and information speckle is difficult [10] we need not be concerned. We are

only interested in the gross anatomical structure of the retina and optic nerve head and not in its microstructure. Thus both types of speckle can be considered noise for our case.

While some speckle can be reduced through imaging techniques such as spatial compounding and polarization diversity there still remains a significant problem. Because of its signal dependent nature, speckle noise can not readily be decoupled from the signal. Various techniques have been proposed to alleviate the problem with the most common being the use of median filtering [13, 14, 11] or one of its variations. Suvichakorn and Chinrungrueng propose fitting a two-dimensional polynomial using a least squares approach to estimate the actual image intensities [15]. Park et al. rely on an adaptive windowing procedure with adpative filtering based on local statistics [16] and Xiang et al. used wavelet filters incorporating automatic noise thresholds [17].

Observations of retina and optic nerve images reveal that there is a significant contrast difference at the vitreal-retinal boundary. When speckle is suppressed through filtering, the retina becomes a relatively homogenous region and the contrast between the vitreous humor and retina is significantly increased. Define Region 1 to be the vitreous humor and the dark area in the lower portion of the image corresponding to signal loss. Next, define Region 2 as the retina, optic disk, and choroid. Now we assume that there exists a threshold t such that Region 1 is completely separated from Region 2. If such a t exists then the top profile of the retina and optic nerve is just the boundary between the upper portion of Region 1 and Region 2.

Thresholding is a simplistic yet powerful image segmentation tool. The problem with thresholding lies in the selection of the threshold. Assuming that the pixel distributions of the regions are normal, one might consider using Otsu's thresholding algorithm [18] which seeks to minimize the within class variance of the two distributions in a bimodal histogram. This can provide sub-optimal results if there is considerable overlap between the distributions or if the histogram is not bimodal. Rather than rely on the histogram to select the threshold we propose a new method based on edge maximization and smoothness constraints to choose an optimal threshold.

Let E(r,c) be an edge image produced by column-wise, one-dimensional edge detection, r(t,c) be the boundary of interest as a function of the threshold t and image columns, and r'(t,c) be the first derivative with respect to c. Note here that E(r,c) may be a modification of the actual edge image, for instance we could threshold the weaker edges or use only edges of a certain polarity. Furthermore, define p(t,c) to be a function that corresponds to whether an edge exists (we could also use edge strength) for a given r(t,c), that is

$$p(t,c) = E(r(t,c),c) \tag{3}$$

Now we can define a cost function

$$J(t) = \sum_{c} p(t,c) - \alpha \frac{1}{N_c} \sum_{c} |r'(t,c)|$$
 (4)

where α is a constant of proportionality. The optimal threshold given the criteria we have defined can then be found by setting

$$\frac{\partial J}{\partial t} = 0 \tag{5}$$

and solving for t.

The first term of (4) corresponds to the number of edge locations that intersects r(t,c). The second term adds a smoothness constraint based on the anatomical properties of the vitreal-retinal boundary. We expect that the average rate of change of the correct boundary is small (even in the region of the optic cup). Breaks in the boundary due to subject movement or portions of the optic cup may correspond to a high rate of change. However, this will be relative constant over a range of thresholds and should not affect the correct choice of t. This terms adds a degree of robustness to J(t) particularly in the case of shadowing. In A-scans where there is partial occlusion the contrast tends to be lower than the non-occluded A-scans and the second term tends to pull the threshold lower to account for the occlusion. The constant α controls the amount of correction that can occur. Setting α too low results in little or no correction while setting α too high can cause incorrect segmentation. Thus the optimal t maximizes the number of edge locations in E(r,c) located along r(t,c) and minimizes the average rate of change of r(t,c).

Fig. 2A shows an OCT image where the noise has been suppressed by median filtering. Fig. 2B shows the histogram of the image along with Otsu's threshold and the threshold chosen by our algorithm. In this case the distributions do not clearly exhibit a bimodal nature. Fig. 2C shows the result of thresholding based on Otsu's method. Fig. 2D shows the result of minimizing J(t) to obtain the correct threshold.

At first glance (4) resembles the active contour model first proposed by Kass et al. [19] and seen extensively throughout the literature [20, 21, 22, 23]. Indeed, there are some similarities since we are seeking a threshold dependent upon image forces and contour smoothness. The key difference lies in that we have defined a function J(t) in terms of a scalar threshold t. Active contour models seek an entire contour the minimizes a certain functional. In our case, the contour results from finding the threshold that minimizes J(t). Indeed, (4) is less sophisticated and simpler than the active contour model but it suffers less from some of the problems associated with active contour models such as contour initialization and attraction to incorrect minima.

The vitreal-retinal boundary Y(x) can be modeled as a piecewise smooth function consisting of a straight line segment, followed by a parabolic segment, and ending with another straight line segment as follows:

$$P(x) = \begin{cases} a_1 x + b_1 & \text{if } c_1 \le x \le c_2 \\ a_2 x^2 + b_2 x + c & \text{if } c_2 \le x \le c_3 \\ a_3 x + b_3 & \text{if } c_3 \le x \le c_4 \end{cases}$$
 (6)

while c_1 and c_4 are known since they represent the first and last columns in the image, c_2 and c_3 are unknowns which we will call breakpoints. The parameters

for each curve segment are also unknown, but if we are given c_2 and c_3 , the parameters for each curve segment can be found using a least squares fit. For instance, in the case of the parabolic segment one needs to solve the matrix equation

$$\begin{bmatrix} x_1^2 & x_1 & 1 \\ x_2^2 & x_2 & 1 \\ \vdots & \vdots & \vdots \\ x_N^2 & x_N & 1 \end{bmatrix} \begin{bmatrix} a_2 \\ b_2 \\ c \end{bmatrix} = \begin{bmatrix} P_1 \\ \vdots \\ P_N \end{bmatrix}$$
 (7)

where x_i and P_i are defined in (6). The solution to (7) is

$$\begin{bmatrix} a_2 \\ b_2 \\ c \end{bmatrix} = (X^T X)^{-1} X P \tag{8}$$

where we have used the Moore-Penrose inverse. The parameters for each segment can thus be found provided that c_2 and c_3 are known but the problem is that c_2 and c_3 are not known. In order to find the breakpoints we will need to define a criterion that will provide insight to how well P(x) for a given c_2 and c_3 models the boundary profile Y(x). First let

$$\bar{\mathbf{c}} = \begin{bmatrix} c_2 \\ c_3 \end{bmatrix} \tag{9}$$

Next, consider

$$P_i(x) = P(x) \ c_i \le x \le c_{i+1}$$
 (10)

to represent the modeled boundary using the parameters from (6) where i represents the curve segment number. Also define

$$Y_i(x) = Y(x) \ c_i < x < c_{i+1}$$
 (11)

Then we can write the squared error for each curve segment as

$$e_i(\overline{\mathbf{c}}) = \sum_{n=c_i}^{n=c_{i+1}} (Y_i(n) - P_i(n))^2 \quad i = 1...3$$
 (12)

Now we can write the total squared error, TE, as a function of $\bar{\mathbf{c}}$

$$TE(\bar{\mathbf{c}}) = \sum_{i=1}^{3} e_i(\bar{\mathbf{c}}) \tag{13}$$

 $TE(\bar{\mathbf{c}})$ gives us an indication of how well our model fits the actual upper retina-optic nerve head profile for a given set of breakpoints. Now we assume that $TE(\bar{\mathbf{c}})$ has a global minimum that corresponds to the ideal location of the breakpoints. That is, when $TE(\bar{\mathbf{c}})$ is minimized, the model we have proposed has found the edges of the optic cup. Here we will make one further assumption about $TE(\bar{\mathbf{c}})$, that is the error function is quadratic and only has one minimum. This is of course a weak assumption. In actuality there are saddle points and local minima on the error surface; however, these local minimum and saddle points are usually much weaker then the global minimum and thus the assumption that $TE(\bar{\mathbf{c}})$ is a quadratic error surface is justified. Since we assume that $TE(\bar{\mathbf{c}})$ is quadratic we can then use a gradient descent algorithm to locate the correct breakpoints.

4 The Algorithm

4.1 Median Filtering (Step 1)

The first step in our approach is noise suppression. We chose to use a median filter due to its simplicity and its property of preserving the important macrostructure of the image. We applied a 4 x 4 median filter to each image twice. This suppresses most of the speckle and homogenizes the retina and choroid by destroying the underlying microstructure. Because the columns of an image are acquired independently, two-dimensional median filtering tends to introduce artifacts. However, since we are only relying on the edges to choose a threshold, the artifacts are of little consequence. The result of filtering can be seen in Fig. 2A.

4.2 Columnwise Edge Detection (Step 2)

Edge detection was performed on the each A-scan of the filtered image. The lack of registration, the speckle character of the noise, and the dislocations between adjacent columns tend to cause problems in the case of 2-D kernels. Indeed, the transverse and axial resolutions are not identical whereas most 2D kernels are isptropic and rely on the assumption that the transverse and axial resolutions are identical. Columnwise edge detection is similar to the methods of Thune $et\ al.[24]$ and Koozekanani $et\ al.[11]$.

We chose to use the Marr-Hildreth operator (LoG) which is given below [25]. There is no special reason for this choice as any other 1D kernel, such as the optimal zero-crossing operator proposed by Sarkar and Boyer [26], would have worked as well.

$$E(r) = g''(r) * A \tag{14}$$

where

$$g(r) = \exp(\frac{-r^2}{2\sigma^2}) \tag{15}$$

The edge locations $s_{zc}(r)$, are the zeros crossings of (14). We chose to use a $\sigma=5$. This provided a compromise between edge position preservation and additional filtering of noisy edges. Edge preservation is particularly important as threshold choice relies on the assumption that a large number of edges lie on the vitreal-retinal border. We can reduce the number of edges in the image by considering only those edges of negative polarity. This is justified because the vitreal-retinal border is a transition from a darker region to a lighter region.

4.3 Optimal Threshold Selection (Step 3)

Using the cost function that we defined in (7) we wish to learn which threshold value t extremizes this function. In this case a gradient descent algorithm can be computationally expensive and slow to converge and is thus undesirable. Instead we sample J(t) for a set of t values which are evenly spaced over a range that typically bounds t. Our observations, over many trials, indicate that J(t)

is generally a well behaved parabolic function for the bounded set of threshold values. We then fit a parabola to the sampled J(t) and the extremum for

$$y(t) = at^2 + bt + c (16)$$

occurs at

$$t = -\frac{b}{2a} \tag{17}$$

This is the optimal threshold according to our definition of J(t).

4.4 Boundary Extraction (Step 4)

Using t as found in Step 3 to threshold the image, the matter of boundary extraction is trivial. Noise in the vitreous humor can cause small artifacts to occur in this region of the thresholded image. These are easily removed and the boundary is just the first non-zero pixel in each image column.

4.5 Curve Segmentation (Step 5)

Given the retina-optic disk boundary from Step 4, the final step of our algorithm is to find the edges corresponding to the optic cup in the boundary. Using the model we stated earlier (6) and the cost function (13) we can use a gradient descent algorithm to find the columns that best correspond to the edges of the optic cup. The method of gradient descent updates the current estimate of $TE(\bar{\mathbf{c}})$ for each iteration k by

$$\bar{\mathbf{c}}(k+1) = \bar{\mathbf{c}}(k) - \eta \nabla T E(\bar{\mathbf{c}}, k) \tag{18}$$

where η is called the learning rate. The gradient descent algorithm moves along the negative direction of the gradient until the algorithm converges to the optimal value of $TE(\bar{\mathbf{c}})$. The parameter η controls the speed of convergence; however, if η is set too high divergence may occur. Although methods exist to calculate the best η and to update it iteratively, we found that $\bar{\mathbf{c}}$ typically converged quickly even for small values of η and by making η smaller we can avoid divergence problems. Limitations of this method occur if patient movement is significant enough to severely alter the retina profile. In this case the model that we chose no longer fits the actual profile.

5 Results

The algorithm generally identified the correct vitreal-retinal boundary in the images. The rare exceptions occur when the OCT signal has been severely attenuated due to shadowing. If the shadowing is severe enough in a portion of an image, then the threshold selected will set all of the A-scans affected by the shadowing to zero. In this case, no boundary will be found; however, it is easily identified and measures can be attempted to find the correct boundary.

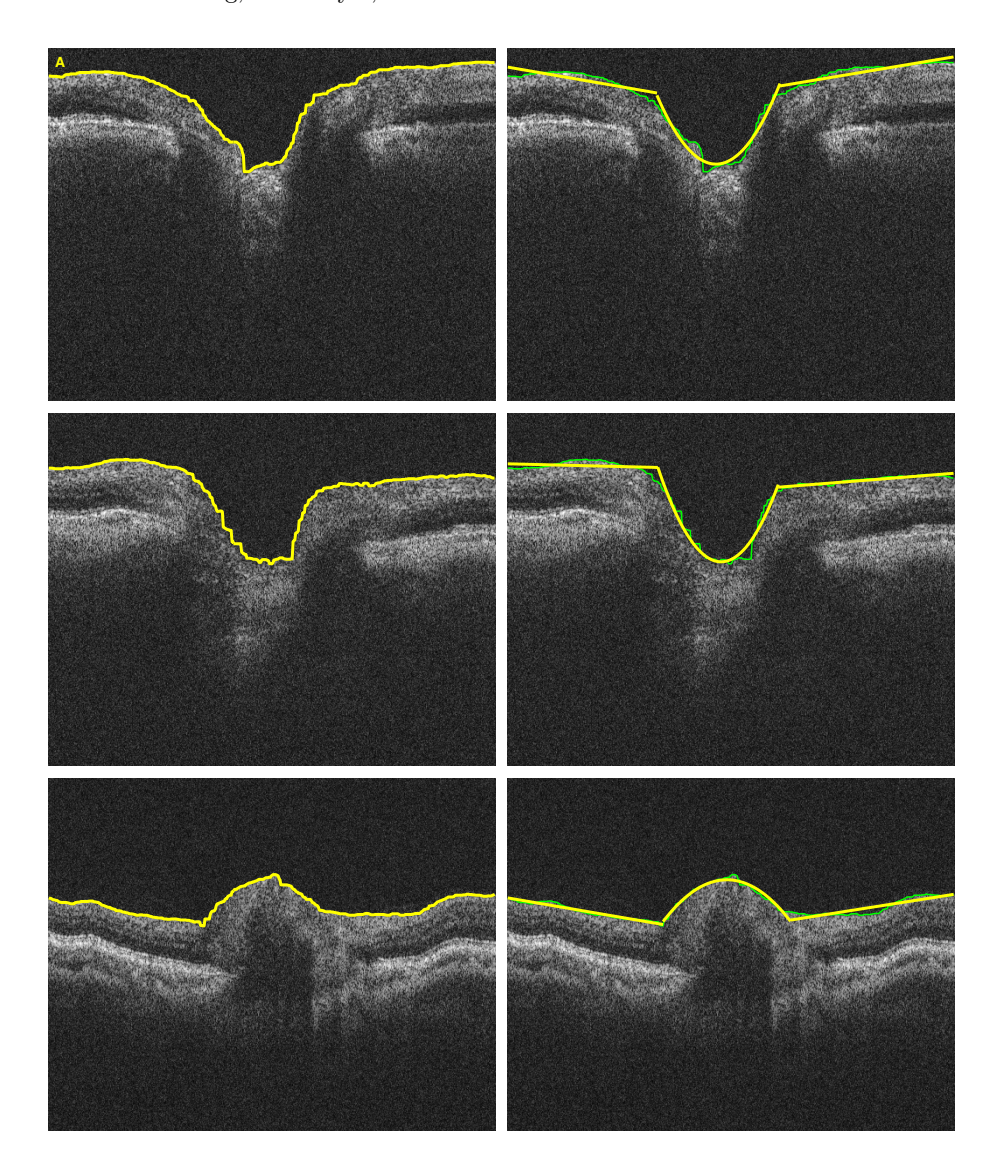


Fig. 3. (A) shows an example of a correctly identified boundary while (B) shows the resulting curve segmentation. (C) and (D) show another pair with correct boundary identification and segmentation. (E) and (F) show the results for a subject suffering from papilla edema. Again we have identified the correct boundary and have achieved correct segmentation.

Our curve segmentation algorithm also produced good results. Exceptions occurred when movement introduced a significant distortion in the boundary profile. Fig. 3 shows some examples of results obtained using our algorithm.

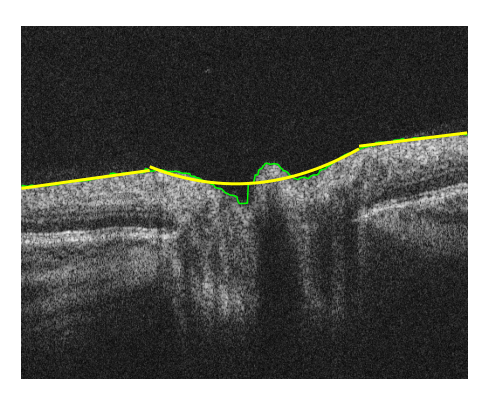


Fig. 4. An example where the boundary curve is not segmented properly due to distortion from subject movement.

Fig. 4 shows an example of curve segmentation when the boundary profile has been affected due to movement.

6 Conclusion

We have presented two significant contributions in this paper. First, we have developed a method to adaptively threshold OCT images of the optic disk in order to extract the vitreous-retinal boundary from the images. Our method relies on maximizing the number of edges that lie on the boundary while minimizing the boundary's average rate of change. Our method proves to be robust even in the presence of noise artifacts and significant shadowing that would normally cause problems in identifying the correct boundary. The second contribution is an accurate segmentation of the boundary profile obtained via our thresholding technique. This curve parsing procedure relies on a piecewise continuous model of the retinal-boundary where the retina/optic disk portions of the boundary are represented as straight lines and the cup portion is represented by a parabola. By minimizing the sum of squared errors for each segment we can find the optimal edge points of the optic cup. Reliable boundary extraction and segmentation of the axial optic nerve head scans are particularly useful in the clinical setting where current diagnostic procedures lend themselves to the subjectivity of the technician. Further work includes finding the boundary regions corresponding specifically to the optic disk so that a cup-to-disk ratio can be calculated and used in a clinical setting.

References

Huang, D., Swanson, E.A., Lin, C.P., et al.: Optical coherence tomography. Science 254 (1991) 1178–1181

- [2] Welzel, J., Lankenau, E., Birngruber, R., Engelhardt, R.: Optical coherence tomography of the human skin. J. Am. Acad. Derm 37 (1997) 958–963
- [3] Brezinski, M.E., Tearney, G.J., Brett, B.E.: Imaging of coronary artery microstructure with optical coherence tomography. American Journal of Cardiology 77 (1996) 92–93
- [4] Hee, M.R., Izatt, J.A., Swanson, E.A., et al.: Optical coherence tomography for ophthalmic imaging. IEEE Engineering in Medicine and Biology 14 (1995) 67–76
- [5] Wang, R., Koozekanani, D., Roberts, C., Katz, S.: Reproducibility of retinal thickness measurements using optical coherence tomography. Investigative Ophthalmology and Visual Science 40 (1999) S125–S125
- [6] Zeiss-Humphrey: Optical coherence tomographer model 3000: User manual (2002)
- [7] Puliafito, C.A., Hee, M.R., Schuman, J.S., Fujimoto, J.G., eds.: Optical Coherence Tomography of Ocular Diseases. First edn. Slack, Thorofare (1996)
- [8] Boyd, B.F., Luntz, M.H., eds.: Innovations in the Glaucomas: Etiology, Diagnosis, and Management. First edn. Highlights of Ophthalmology Int'l, El Dorado (2002)
- [9] Tasman, W., Jaeger, E.A., eds.: The Willis Eye Hospital Atals of Clinical Ophthalmology. 2nd edn. Lippincott and Williams and Wilkins, Philadelphia (2001)
- [10] Bouma, B., Tearney, G.J., eds.: Handbook of Optical Coherence Tomography. 1st edn. Dekker, USA (2001)
- [11] Koozekanani, D., Boyer, K., Roberts, C.: Retinal thickness measurements in optical coherence tomography using a markov boundary model. In: IEEE Computer Society Conference on Computer Vision and Pattern Recognition. Volume 2., Hilton Head, SC (2000) 363–370
- [12] Schmitt, J.M.: Optical coherence tomography (oct): A review. IEEE Journal of Selected Topics in Quantum Electronics 5 (1999) 1205–1215
- [13] Loupas, T., McDicken, W.N., Allan, P.L.: An adpative weighted media filter for speckle suppression in medical ultrasonic images. IEEE Transactions on Circuits and Systems 36 (1989) 129–135
- [14] Czerwinski, R.N., Jones, D.L., Jr, W.D.O.: Ultrasound speckle reduction by directional median filtering. In: Proceeding of the 1995 International Conference on Image Processing. Volume 1. (1995) 358–361
- [15] Suvichakorn, A., Chinrungrueng, C.: Speckle noise reduction for ultrasound images. In: IEEE APCCAS 2000. (2000) 430–433
- [16] Park, J.M., Song, W.J., Pearlman, W.A.: Speckle filtering of sar images based on adaptive windowing. In: Visual Image Signal Processing. Volume 146. (1999) 430–433
- [17] Xiang, S.H., Zhou, L., Schmitt, J.M.: Speckle noise reduction for optical coherence tomography. In: Proc. SPIE. Volume 3196. (1997) 79–88
- [18] Otsu, N.: A threshold selection method from gray level histograms. IEEE Transactions on Systems, Man, and Cybernetics 9 (1979) 62–66
- [19] Kass, M., Witkin, A., Terzopoulos, D.: Snakes: Active contour models. International Journal of Computer Vision (1988) 321–331
- [20] Berger, M., Mohr, R.: Towards autonomy in active contour models. In: IEEE: 10th International Conference on Pattern Recognition, Piscataway NJ (1990) 847–851
- [21] Cohen, L.D.: On active contour models and balloons. In: CVGIP Image Understanding. Volume 53. (1991) 211–218
- [22] Duta, N., Sonka, M.: Segmentation and interpretation or mr brain images using an improved knowledge-based active shape model. In Duncan, J., Gindi, G., eds.: Information Processing in Medical Imaging, Berlin, Springer Verlag (1997) 375–380

- [23] Xu, C., Prince, J.L.: Snakes, shapes, and gradient vector flow. IEEE Transactions of Image Processing 7 (1998) 359–369
- [24] Thune, M., Olstad, B., Thune, N.: Edge detection in noisy data using finite mixture distribution analysis. Pattern Recognition **30** (1997) 685–699
- [25] Marr, D., Hildreth, E.: Theory of edge detection. Proceedings Royal Society, London 2076 (1980) 187–217
- [26] Sarkar, S., Boyer, K.: Optimal impulse response zero crossing based edge detectors. Computer Vision Graphics Image Process: Image Understanding 54 (1991) 224–243